Journal of Biomedical Optics

SPIEDigitalLibrary.org/jbo

Intrinsic photosensitizer fluorescence measured using multi-diameter single-fiber spectroscopy *in vivo*

Floor van Leeuwen-van Zaane
Ute A. Gamm
Pieter B. A. A. van Driel
Thomas J. Snoeks
Henriette S. de Bruijn
Angelique van der Ploeg-van den Heuvel
Henricus J. C. M. Sterenborg
Clemens W. Löwik
Arjen Amelink
Dominic J. Robinson

SPIE

Intrinsic photosensitizer fluorescence measured using multi-diameter single-fiber spectroscopy *in vivo*

Floor van Leeuwen-van Zaane,[a,†] Ute A. Gamm,[a,†] Pieter B. A. A. van Driel,[b] Thomas J. Snoeks,[b] Henriette S. de Bruijn,[c] Angelique van der Ploeg-van den Heuvel,[c] Henricus J. C. M. Sterenborg,[a] Clemens W. Löwik,[b] Arjen Amelink,[a] and Dominic J. Robinson[c,*]

[a]Postgraduate School Molecular Medicine, Center for Optical Diagnostics and Therapy, Department of Radiation Oncology, Erasmus MC, P.O. Box 2040, 3000 CA Rotterdam, The Netherlands

[b]Leiden University Medical Centre, Department of Radiology, P.O. Box 9600, 2300 RC Leiden, The Netherlands

[c]Center for Optical Diagnostics and Therapy, Department of Otolaryngology—Head and Neck Surgery, Erasmus MC, P.O. Box 2040, 3000 CA Rotterdam, The Netherlands

Abstract. Quantification of fluorescence *in vivo* is complicated by the influence of tissue optical properties on the collected fluorescence signal. When tissue optical properties in the measurement volume are quantified, one can obtain the intrinsic fluorescence, which equals the product of fluorophore absorption coefficient and quantum yield. We applied this method to *in vivo* single-fiber fluorescence spectroscopy measurements on mouse tongue, skin, liver, and oral squamous cell carcinoma, where we detected intrinsic fluorescence spectra of the photosensitizers chlorin e6 and Bremachlorin at $t = [3, 4.5, 6, 24, 48]$ h incubation time. We observed a tissue-dependent maximum of 35% variation in the total correction factor over the visible wavelength range. Significant differences in spectral shape over time between sensitizers were observed. Although the wavelength position of the fluorescence intensity maximum for ce6 shifted to the red, Bremachlorin showed a blue shift. Furthermore, the Bremachlorin peak appeared to be broader than the ce6 fluorescence peak. Intrinsic fluorescence intensity, which can be related to photosensitizer concentration, was decreasing for all time points but showed significantly more Bremachlorin present compared to ce6 at long incubation times. Results from this study can be used to define an optimal treatment protocol for Bremachlorin-based photodynamic therapy. [DOI: 10.1117/1.JBO.19.1.015010]

Keywords: intrinsic fluorescence; fiber-optics; spectroscopy; chlorin e6; pharmacokinetics; tissue characterization.

Paper 130730R received Oct. 8, 2013; revised manuscript received Dec. 24, 2013; accepted for publication Dec. 30, 2013; published online Jan. 29, 2014.

1 Introduction

In-vivo optical spectroscopy has been under investigation both as a diagnostic tool and as a method for monitoring a number of therapeutic modalities.[1–4] Reflectance spectroscopy provides information on the presence and concentration of tissue absorbers, while scattering can be related to information on morphology and ultrastructure of tissue.[5,6] Fluorescence spectroscopy enables the detection of endogenous molecules such as collagen and NADH, as well as exogenous fluorophores such as fluorescent-labeled markers and drugs.[7,8] The shape and intensity of the fluorescence spectrum contain valuable information on fluorophore identity, its concentration and the local environment. The interrogation of fluorescent drugs in various tissue types is one of the major applications of *in-vivo* fluorescence spectroscopy and has been widely incorporated in photodynamic therapy (PDT) research and in clinical practice. Photosensitizing agents are well known for their fluorescent properties. It has been shown that knowledge of photosensitizer fluorescence intensity and/or changes in photosensitizer spectral properties before and during treatment may be related to therapeutic efficacy and can be used to monitor PDT.[9–12]

Despite the potential usefulness of *in-vivo* fluorescence spectroscopy, the exact quantification of fluorescent signals is challenging. When measuring fluorescence *in vivo*, the number of collected photons is strongly influenced by optical properties of the tissue under investigation. The local fluence rate is influenced by tissue optical properties at the excitation wavelength (λ_x), while the number of emitted fluorescence photons detected depends on the optical properties at the emission wavelength (λ_m). We are interested in the intrinsic fluorescence, where the influence of tissue optical properties has been removed from the measured fluorescence spectrum and which can, therefore, be related to the fluorophore absorption coefficient and thereby to fluorophore concentration in which exact knowledge of the fluorophore quantum yield. Intrinsic fluorescence enables quantitative comparison of fluorescence intensity and spectral shape measured on tissues with (different and/or) varying optical properties.

Several methods have been developed previously to extract intrinsic fluorescence spectra in turbid media such as biological tissues. To provide accessibility to various tissues, system designs for *in-vivo* use are generally based on fiber-optic probes. Many techniques combine white light reflection measurements to obtain tissue optical properties with a fluorescence measurement and then use analytical or empirical models[4,13,14] to extract the intrinsic fluorescence. A complication of using optical properties obtained from a reflectance measurement to correct fluorescence data is the discrepancy of measurement geometries between the two. Multifiber fluorescent probes with separate source(s) and detector(s), where the detected light is diffuse

*Address all correspondence to: Dominic Robinson, E-mail: d.robinson@erasmusmc.nl

†Both authors contributed equally to this work.

0091-3286/2014/$25.00 © 2014 SPIE

and the sampling volume is in the order of a cubic millimeter, have been extensively investigated.[3,4,13,15,16] In this geometry, both reflectance and (a large part of the) fluorescent light are diffusely scattered. After determination of the optical properties, an analytical model to retrieve intrinsic fluorescence can be used that is independent of specific probe design. Another approach is to use a source and detection fiber with a small separation distance and therefore probing a much smaller sample volume directly below the fiber tip. In this configuration, the majority of detected reflectance and fluorescence photons have undergone too few scattering events to apply diffusion theory and sample volumes for reflectance and fluorescence differ significantly from each other. Therefore, approaches to remove the influence of optical properties from fluorescence are based on (semi-) empirical models and are usually device-specific and measurement geometry-specific. A specific situation of small source–detector separation is to use a single fiber for illumination and detection of both reflected and fluorescent light.[17–20]

Our group has recently developed a fiber-optic system based on the combination of multi-diameter single-fiber reflectance (MDSFR) spectroscopy and single-fiber fluorescence (SFF) spectroscopy; the former functioning to determine tissue absorption and scattering properties, the latter to detect tissue fluorescence.[21–23] Illumination and detection are performed by a single-optical fiber probe for both reflectance and fluorescence measurements. The measurement volume is confined to shallow depths of the order of the fiber diameter.[24,25] It is shown that acquiring two successive single-fiber reflectance measurements with different fiber diameters (termed MDSFR) enables quantification of both the reduced scattering coefficient and the phase function parameter γ. This parameter is defined as $\gamma = (1 - g_2)/(1 - g_1)$, where g_1 and g_2 are the first and second Legendre moments of the phase function, and has to be included due to the shallow measurement geometry.[21,26] Intrinsic fluorescence can be determined using a semi-empirical model based on Monte-Carlo simulations and phantom studies. This model incorporates the effect of optical properties on local excitation fluence and fluorescence photon escape probability within the whole sample volume.[23,27]

An important application field, where measurement of intrinsic fluorescence is particularly valuable, is the determination of photosensitizer fluorescence before and during PDT. Since oxygen is depleted during PDT, saturation levels in the measurement volume change, and hence the optical properties. Other direct effects of PDT include changes in blood volume fraction and vessel diameter influencing absorption and the onset of acute edema, which influences scattering.[11,28–30] Intrinsic fluorescence allows for reliable quantification and comparison of photosensitizer fluorescence at various time points before, during, and after PDT.

Chlorins are a class of second generation photosensitizers that exhibit low dark toxicity and have enhanced absorption in the optical window between 600 and 800 nm. Chlorin e6 (ce6) is a member of this family of photosensitizers and has been studied intensively for over two decades.[31–33] Preclinical studies comparing localization and phototoxicity of ce6 with other photosensitizers are performed.[34,35] Ce6-PVP, in which the ce6 molecule is bound to a polyvinylpyrrolidone carrier, is used in PDT of urological oncological lesions.[36] The second-generation photosensitizer mono-L-aspartylchlorin-e6 has been used successfully in phase I studies for cutaneous lesions,[37] solid tumors,[38] and mucosal surfaces.[39] It is shown that *in-vitro* analysis of cellular uptake of ce6 has a strong dependence of spectral shape on pH of the solution, resulting in a shift of both the absorption and fluorescence spectrum and a decrease of fluorescence intensity.[32,33] By analyzing both intensity and spectral shape, we should be able to distinguish between intensity decreases due to clearance of the photosensitizer from the tissue, and intensity changes due to relocalization to an environment with a different pH. One important aspect of the use of ce6 is its relatively low lipophilicity; this means that it is metabolized rapidly and cleared from the body quickly via the urinary system. This has advantages in, for example, reducing skin photosensitivity but a short clearance time limits its effective localization in neoplastic tissue. A new photosensitizing compound, Bremachlorin, consists largely (~80%) of ce6, combined with the photosensitizing agents purpurin 5 (~15%) and chlorin p6 (~5%).[40,41] The main active component of Bremachlorin is thought to be purpurin 5 because of its rapid interaction with albumin and low-density lipoproteins that enables it to be delivered to cancerous tissues.[42] Although purpurin 5 in itself is too hydrophobic to be administered in aqueous solution, combined with ce6 and cp6, it achieves the chemical stability required for both intravenous administration and storage. It is expected that the combined purpurin 5 and ce6 in Bremachlorin results in an overall photosensitizing effect that is greater than the individual concentrations of both photosensitizers.[40]

In the present study, we have, for the first time, used quantitative SFF spectroscopy *in vivo* to analyze fluorescence spectra of both ce6 and Bremachlorin *in vivo*. Analysis of variations in both fluorescent spectral shape and intensity yields information on clearance and localization of both photosensitizers under investigation. This analysis is applied on healthy tongue tissue, oral squamous cell carcinoma tissue at the tip of the tongue, skin, and liver, for time points ranging from 3 to 48 h after photosensitizer injection.

2 Materials and Methods

2.1 *Correction Theory*

To measure intrinsic fluorescence, it is necessary to correct the measured raw fluorescence signal for the influence of μ_s' and μ_a. The method of determining μ_s' and μ_a from MDSFR spectra has been described in detail elsewhere.[21,22,43] Furthermore, a semi-empirical model is developed, based on Monte-Carlo simulations and phantom studies to account for the influence of tissue optical properties on a fluorescence signal.[23,27] To obtain the fluorescence in the absence of absorption F_{SF}^0 from the measured fluorescence F_{SF}, a modified form of Beer's law is used.[27]

$$F_{\mathrm{SF}} = F_{\mathrm{SF}}^0 e^{(-\mu_{a,\mathrm{avg}}\langle L_{\mathrm{SFF}}\rangle)}. \tag{1}$$

Here, $\mu_{a,\mathrm{avg}}$ is the average μ_a at the excitation and emission wavelengths and the fluorescence photon path length L_{SFF} is defined as

$$\langle L_{\mathrm{SFF}}\rangle = \langle Z\rangle \frac{1 + \kappa\sqrt{(\mu_{s,\mathrm{avg}}' d_f)}}{1 + (\mu_{a,\mathrm{avg}}' d_f)}, \tag{2}$$

where $\mu_{s,\mathrm{avg}}'$ is the average μ_s' at excitation and emission wavelengths, d_f is the fiber diameter and κ represents a single-fitted parameter, which has a value of $\kappa = 1.81 \pm 0.01$.[23] Z is the effective sampling depth, defined as

$$\langle Z \rangle = d_f A_2 (\mu'_{s,\mathrm{avg}} d_f)^{-A_3}, \tag{3}$$

and can be related to the effective sampling volume

$$\langle V \rangle = A_1 \langle Z \rangle d_f^2.$$

In this equation, A_1 is a proportionality factor that depends on the geometrical shape of the effective volume, and A_2 and A_3 are determined empirically to be 0.71 ± 0.01 and 0.36 ± 0.01, respectively.[23,27]

A model is previously developed to relate F^0_{SF} to the intrinsic fluorescence spectrum $F(\lambda_m)$ ($\mathrm{nm}^{-1}\,\mathrm{mm}^{-1}$), which is the product of fluorophore absorption coefficient $\mu_a^f(\lambda_x)$ and quantum yield at the emission wavelength $Q^f(\lambda_m)$,[27]

$$F^{\mathrm{SF}}_{\mathrm{Ratio}} = \frac{F^0_{\mathrm{SF}}}{P_{\mathrm{Laser}}} \approx \left(\frac{\lambda_x}{\lambda_m}\right) \mu_a^f Q^f \langle \phi_x^V \rangle \langle H_m^V \rangle \langle V \rangle. \tag{4}$$

Here, $\langle V \rangle$, $\langle \phi_x^V \rangle$, and $\langle H_m^V \rangle$ are the effective sampling volume, excitation fluence, and escape probability, respectively, which can all be described as a function of μ_s' and d_f. The factor λ_x/λ_m accounts for difference in photon energy between emission and excitation wavelength. $F^{\mathrm{SF}}_{\mathrm{Ratio}}$ is the ratio between the total excitation photons launched (related to P_{laser}) and the emitted photons detected (related to F^0_{SF}). The product of Eq. (4) and the expressions for $\langle V \rangle$, $\langle \phi_x^V \rangle$, and $\langle H_m^V \rangle$ yields

$$\frac{F^{\mathrm{SF}}_{\mathrm{Ratio}}}{\mu_a^f Q^f d_f V_f} \left(\frac{\lambda_m}{\lambda_x}\right) = \zeta_1 (\mu'_{s,\mathrm{avg}} d_f + 0.00315)^{\zeta_2} e^{\left\{\frac{-1}{\zeta_2 [\mu'_s(\lambda_x) d_f]+1} - \frac{\zeta_3}{\zeta_2 [\mu'_s(\lambda_m) d_f]+1}\right\}}, \tag{5}$$

where $[\zeta_1 \;\; \zeta_2 \;\; \zeta_3]$ are fitted parameters with values $[0.0935 \pm 0.003,\ 0.31 \pm 0.01,\ 1.61 \pm 0.05]$ and λ_x and λ_m are the excitation and emission wavelengths, respectively.[27] Since our measurements, and therefore, the intrinsic fluorescence spectra did not only contain photosensitizer fluorescence but also include autofluorescence and green fluorescent protein (GFP) fluorescence in measurements on tumor tissue, the contribution of the latter two to the intrinsic fluorescence spectra was determined by spectral deconvolution and both components were subtracted, resulting in photosensitizer intrinsic fluorescence spectra. We note that Eq. (5) includes a value of 0.00315 to be able to apply the model in the very low scattering regime. Including this factor results in a theoretical maximum value for Eq. (4) of 0.041 for $\mu_s' = 0\ \mathrm{mm}^{-1}$, which corresponds with the analytically derived maximum fluorescence in the situation of no scattering and no absorption using a NA = 0.22 fiber in a medium with a refractive index of $n_0 = 1.33$.[44]

2.2 *Measurement Setup*

The illustration in Fig. 1 represents a single-probe unit of the combined MDSFR-SFF spectroscopic setup. Two of those probe units were used, with the only difference in fiber diameter of the probe and quadfurcation, to be able to perform measurements with both 0.4 and 0.8 mm probes. Positioning of the probes was done manually.

The measurements consisted of subsequent reflectance and fluorescence measurements without probe repositioning.

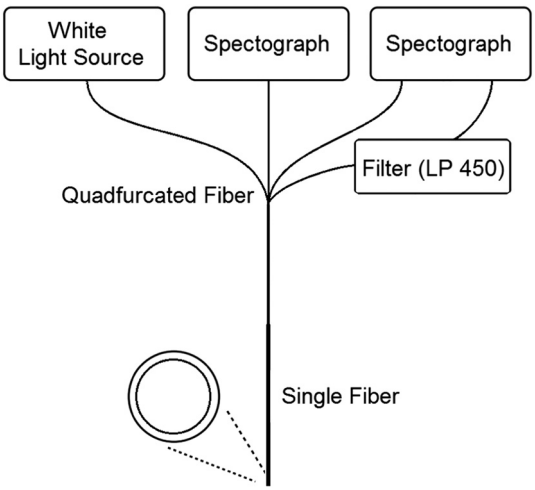

Fig. 1 Schematic diagram of the measurement setup. Reflectance and fluorescence are measured through a single fiber of either 0.4 or 0.8 mm. Two identical setups are used to accommodate the two fiber diameters.

During a reflectance measurement, white light emitted by a halogen light source (HL-2000-FHSA; Ocean Optics, Duiven, Netherlands) was directed through the first leg of a quadfurcation into a solid core fiber-optic probe and guided onto the tissue. A small fraction of the white light was reflected from the tissue into the acceptance cone of the probe fiber and directed via a second leg of the quadfurcation into a spectrometer (SD-2000; Ocean Optics] for detection and further analysis. After the reflectance measurement, the fluorescence measurement was performed, using low power 405-nm excitation light coupled into one leg of the quadfurcation to illuminate the tissue through the same solid core probe as the reflectance. The emitted fluorescence was then guided through the last leg of the quadfurcation, which leads through a 450-nm long-pass filter into a second spectrograph (QE-65000; Ocean Optics) by the use of a solid core 0.2-mm fiber. The complete MDSFR-SFF system consists of two identical probe-units containing probe core diameters of 0.4 and 0.8 mm, combined with a 4×0.1 mm and a 4×0.2 mm quadfurcation, respectively. The fiber probes were sequentially placed in contact with the tissue under investigation. Both probes were polished under an angle of 15 deg to minimize internal specular reflections from the probe tip. The calibration procedure using a diluted Intralipid 20% phantom included correction for fiber alignment and transmission efficiency and is described elsewhere.[45]

2.3 *Animal Model*

For this study, 19 mice (BALB/c nu/nu female mice, aged 4 to 6 weeks; Charles River Laboratories, Chatillon-sur-Chalaronne, France) were injected metastatic oral squamous cell carcinoma cell line OSC19. This cell line has been lentivirally transfected with luc2 (Biocat, Heidelberg, Germany) and Cop-GFP (Evrogen, Moscow, Russia). 6×10^4 cells, diluted in 20-μl phosphate buffered saline (PBS), were injected to induce an oral squamous cell carcinoma at the tip of the tongue after an incubation period of 10 to 13 days.[43,46–48] GFP was included in the cell line to easily assess the inclusion of tumor tissue in the measurement volume. After tumor incubation, animals were restrained and injected with chlorin e6 (16 mg/kg in 100-μl

PBS, Frontier Scientific, Inc., Logan, Utah) or Bremachlorin (20 mg/kg, form stock solution of 3.5 $g1^{-1}$, Radapharma International B.V., The Netherlands). At $t = 3$, 4.5, 6, 24 or 48 h after photosensitizer injection, animals were anesthetized with an injection of ketamine/xylazine and spectroscopic reflectance measurements with both fiber diameters and fluorescence measurements with the 0.4-mm fiber were performed on normal tongue tissue, OSC tumor (both five measurements per fiber diameter), skin and liver (both three measurements per fiber diameter), after which the animals were sacrificed. The consecutive measurements were taken by removing and carefully repositioning the fiber between measurements, without imparting undue pressure on each tissue. For tumor, the fiber tip was positioned directly on top of the visible tumor. The study protocol was approved by the Animal Welfare Committee of the Leiden University Medical Center. Housing of BALB/c nu/nu female mice, the experiments and euthanazation were performed in accordance with the guidelines of this committee. Chlorophyll-free food and sterilized water were provided without restriction.

2.4 *Data Analysis*

All data analyses were performed using custom applications running in MATLAB (release 2009b, The Mathworks, Natick, Massachusetts). Reflectance spectra were fitted with a combination of basis spectra by using a Levenberg–Marquart nonlinear fit procedure to estimate μ_a. μ_s' was determined by averaging the absorption-corrected reflectance spectra per fiber diameter and fitting a model through those averaged reflectance spectra of both fiber diameters, as previously described.[43] Individual measurements that were excluded from the MDSFR fit were excluded from SFF analysis as well. Spectra were excluded from the analysis when (1) fluorescence measurements did not indicate the presence of tumor tissue in the tumor measurement, (2) we were unable to fit μ_a to the individual reflectance spectrum, and (3) we could not successfully fit μ_s' or γ to the averaged absorption-corrected reflectance spectra. The fluorescence spectra from all individual measurements were corrected for absorption and scattering as described above. These corrected fluorescence spectra were then divided into autofluorescence, GFP fluorescence, and photosensitizer fluorescence by spectral deconvolution. The autofluorescence and GFP were then subtracted to obtain the intrinsic fluorescence spectrum. Basis spectra for GFP and autofluorescence were constructed from fluorescence measurements on more than five animals before fluorophore injection, where normal tongue and tumor were fitted with an identical autofluorescence spectrum. Skin and liver were both analyzed with their tissue-dependent autofluorescence basis spectrum. Spectral deconvolution was again based on a Levenberg–Marquart nonlinear fit procedure. The resulting intrinsic photosensitizer fluorescence spectrum was related to the product of photosensitizer absorption coefficient and quantum yield $\mu_a^f Q^f$ by integration over wavelength. To quantify variations in the shape of the spectral emission, two Gaussians were fitted to the main ce6/Bremachlorin peak present in the intrinsic photosensitizer fluorescence spectrum; one covering the high-intensity emission peak, fitted between 650 and 680 nm and a skewed Gaussian to determine the width and intensity of the emission shoulder at the right side of the maximum between 680 and 800 nm. This skewed function is defined as

$$f(\lambda) = b_1 \left\{ e^{\left[\frac{-(\lambda-b_2)^2}{2b_3^2}\right]} \left\{ 1 + \mathrm{erf}\left[b_4 \left(\frac{\lambda - b_2}{\sqrt{2}} \right) \right] \right\} \right\}. \quad (6)$$

The parameters b_1 to b_4 were fitted using a least-mean-square method to describe the shape of the right hand sight of the spectra. From these fitted Gaussian curves, we were able to determine the intrinsic fluorescence intensity, peak wavelength, FWHM of both fitted Gaussians, and the ratio between different fit parameters. The underlying reasons for implications of these spectral shifts are discussed below.

3 Results

For this experiment, 299 spectra were included in the analysis. In biological tissue, largest variations of absorption in the visible range are found in the 400 to 600 nm range, while scattering is decreasing with increasing wavelength.

Figure 2 shows a typical example of MDSFR spectra taken on tumor tissue, using a 400- and 800-nm fiber, together with their corresponding scattering background model in the absence of absorption. Around 500 nm, a peak could be distinguished, caused by strong GFP fluorescence of the tongue tumor, excited by white light used to acquire the reflectance spectra.

3.1 *Magnitude of the Correction for Tissue Optical Properties*

The correction factor was calculated over the whole spectral range for both absorption and scattering for the four different tissues, averaged over all mice. These are shown in Figs. 3(a) and 3(b). The error bars indicate the SD of all measurements per tissue. The correction factors were dependent on the tissue type and illustrated the importance of our technique for the recovery of intrinsic fluorescence in different tissue types: absorption was significantly stronger in liver where there was a high concentration of blood, whereas skin had the lowest absorption. Scattering correction did not vary significantly with tissue type [Fig. 3(b)]. The spectral variation of oxygenated and deoxygenated blood was observed in tumor and normal tongue absorption coefficients. The variation in the total correction factor over the visible wavelength range for both the absorption and scattering is

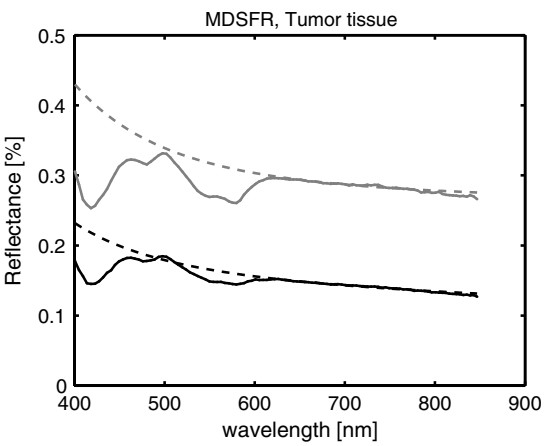

Fig. 2 Reflectance measurement of tongue tumor tissue. Black = 400-nm fiber, Gray = 800-nm fiber. Shown are the reflectance spectrum (solid line) and the scattering background model (dashed line), averaged over five consecutive measurements.

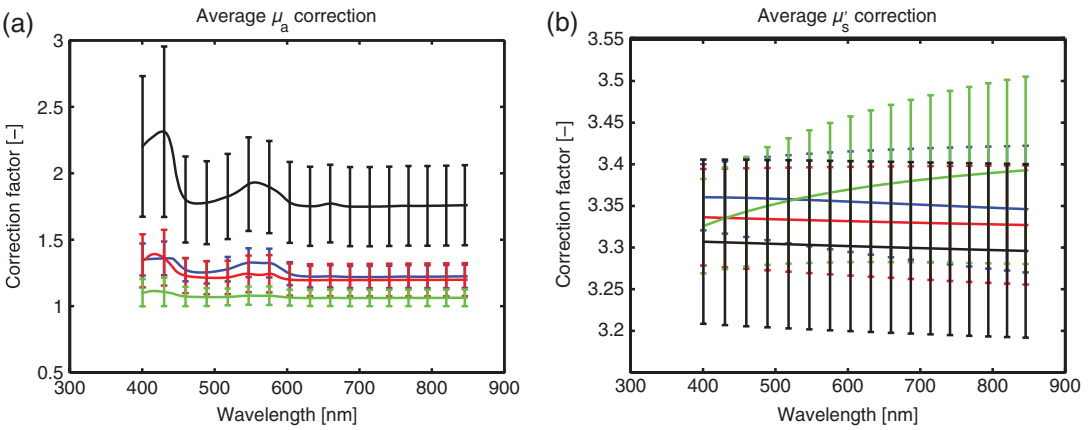

Fig. 3 (a) Average absorption correction factor spectrum for four different tissues. Since the absorption coefficient was wavelength dependent, the absorption correction is, too. Calculation is based on Eq. (1). (b) Average scattering correction factor spectrum for four different tissues, resulting from Eq. (5).

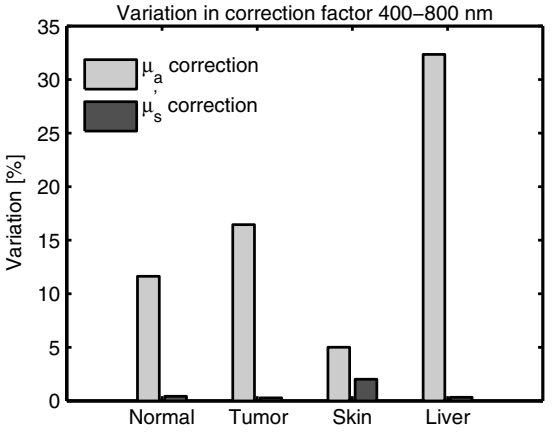

Fig. 4 Variation over the visible wavelength range (400 to 800 nm) of the corrections for absorption and scattering. Maximum value in that range divided by minimum value.

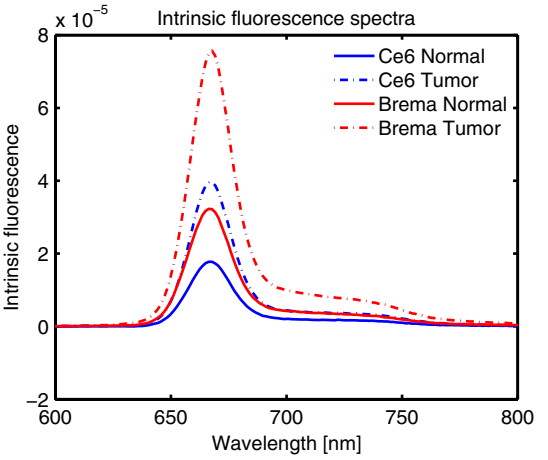

Fig. 5 Typical ce6 and Bremachlorin spectrum in normal tongue and tumor, 3 h after photosensitizer injection.

shown in Fig. 4, where the maximum value of the absorption- or scattering-based correction factor is divided by the minimum value. This figure shows clearly that correction for tissue absorption was most important with regards to analysis of spectral shape. Scattering varied less over wavelength, although the contribution of the scattering correction to the total correction procedure was larger than that of absorption. Therefore, incorrect scattering correction will result in an incorrect quantification of the fluorophore but much less in incorrect conclusions on spectral shape. Applying both absorption and scattering correction results in the intrinsic fluorescence spectrum.

When comparing intrinsic fluorescence spectra of Bremachlorin and ce6 of normal and tongue tumor tissue in Fig. 5, Bremachlorin showed higher fluorescence intensity than ce6 did for both the tissues. Furthermore, the tumor tissue intensity was much higher than that of normal tissue. To illustrate the spectral variations of ce6 and Bremachlorin in different tissues at different time points, Figs. 6(a) and 6(b) show normalized spectra acquired from different tissues and time points. Between 3 and 24 h after injection, the ce6 peak shifted toward longer wavelengths, whereas for Bremachlorin, a shift toward lower wavelengths was measured. Furthermore, clear differences in peak width and the contribution of the longer wavelength shoulder were observed over time after photosensitizer administration.

To quantify these spectral variations in the intrinsic photosensitizer fluorescence spectrum, the fluorescence was characterized by two fitted Gaussian distributions as shown in Fig. 7; one covered the high-intensity emission peak, fitted between 650 and 680 nm and a skewed Gaussian determined the width and intensity of the emission shoulder at the right side of the maximum between 680 and 800 nm.

3.2 *Intensity and Ratio*

Both ce6 and Bremachlorin showed the highest intensity of the intrinsic fluorescence spectrum, hereafter referred to as fluorescence intensity, in liver and lowest in normal tissue. Furthermore, fluorescence intensity of Bremachlorin was significantly higher in all tissues at all time points (except 3 and 6 h measurements in liver, where the difference is not significant), as can be seen in Fig. 8(a). Every bar in Fig. 8 indicates the average measurement value of all measurements taken on all mice for that particular tissue and time point, which corresponds to an average of 6 to 10 measurements. The fluorescence intensity was measured as the maximum value of the fluorophore

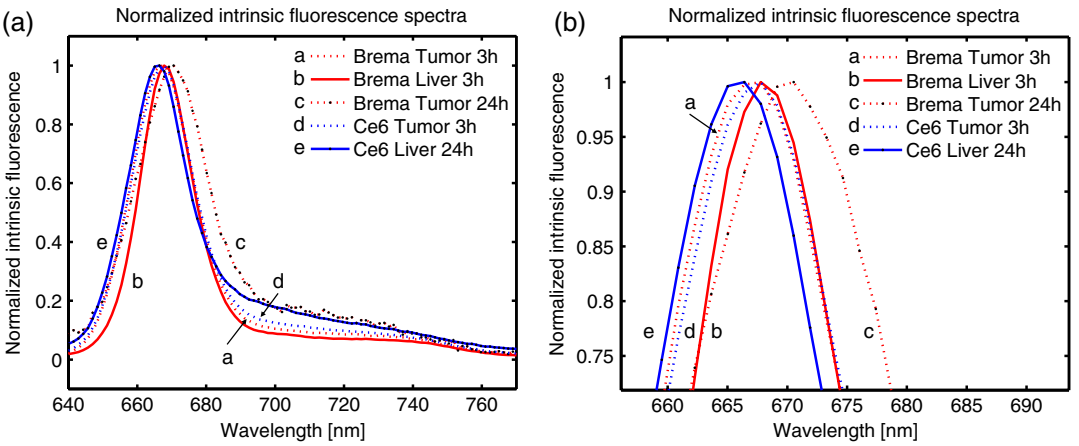

Fig. 6 (a) Characteristic intrinsic photosensitizer fluorescence spectrum for varying tissue, time, and photosensitizer, normalized to peak = 1. (b) Close up of peak position.

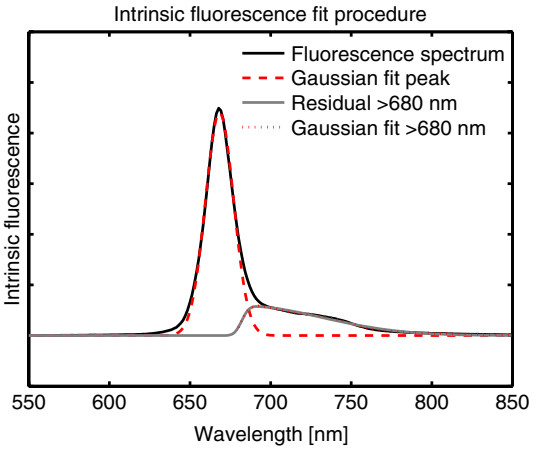

Fig. 7 Fluorescence intensity is fitted with a Gaussian distribution between 650 and 680 nm, and a skewed Gaussian distribution from 680 to 800 nm.

intrinsic fluorescence spectrum. It is evident from the data [Fig. 8(a)] that there was relatively less ce6 present in time as it was cleared more rapidly than Bremachlorin. This may have significant implications for the use of Bremachlorin as a photosensitizer and will be discussed in more detail elsewhere. Figure 8(b) shows the intensity ratio of the main peak and the shoulder on the right side. For this, the maximum values of both fitted Gaussian distributions were divided by each other. Ce6 showed ratios between 8.4 and 11.0, significantly larger than Bremachlorin (ratios between 5.9 and 7.5) for 3, 4.5, and 6 h after injection in all tissues, indicating a lower shoulder for ce6 compared with Bremachlorin ($P < 0.02$ for all time points and tissues). The 24- and 48-h time points were not considered in this analysis because the fluorescence intensity of the shoulder was, in many cases, too low to be fitted accurately. For each photosensitizer, differences over time and tissue were small and rarely significant, as indicated in Fig. 8(b).

3.2.1 *Peak position*

Figure 8(c) shows that the wavelength of the maximum intrinsic fluorescence intensity was shifted more toward the red for ce6 compared with Bremachlorin for tongue tissue, tumor tissue, and skin. The peak position of Bremachlorin ranged from 667 to 665 nm, while ce6 ranged from 665 to 671 nm. This discrepancy was significant ($P < 0.05$) for all time points in normal tongue tissue, tumor tissue, and skin. Liver showed a blue-shift of the peak wavelength over time for both photosensitizers that did not significantly differ from each other for $t = [3, 6, 24]$ h. Bremachlorin showed a decrease of peak position wavelength over time for all four tissues, while, although not always significant, ce6 showed an increasing trend for tongue tissue, tumor, and skin. From Figs. 8(b) and 8(c), we can conclude that for ce6, a shift of the peak to a higher wavelength corresponded with an increase in the peak-shoulder ratio. Possible explanations for the observed wavelength shifts can be found in Sec. 4.

3.3 *Width*

When comparing the width of the main fluorescence emission peak of both photosensitizers in Fig. 8(d), it can be seen that in general the width of the spectrum of ce6 peak was significantly smaller than that of Bremachlorin. It should be noted that the 24 and 48 h measurements of ce6 were associated with large uncertainty caused by the very low fluorescence intensity, compared to Bremachlorin, as shown in Fig. 8(a). This was reflected in an increased fit uncertainty. Over the first 6 h after injection, Bremachlorin showed a stable peak width for all tissues under investigation, whereas ce6 showed a steady but not a significant decrease over time for tumor and normal tissue.

4 Discussion

In this paper, with we have demonstrated for the first time the application of SFF *in-vivo*. We report on variations in spectral shape of the fluorescence emission of two photosensitizers chlorin e6 and Bremachlorin in various tissues after intravenous injection. To compare fluorescence intensity and spectral shape in different tissues and of multiple animals, we extracted the intrinsic fluorescence by removing the influence of tissue optical properties on the raw fluorescence signal.

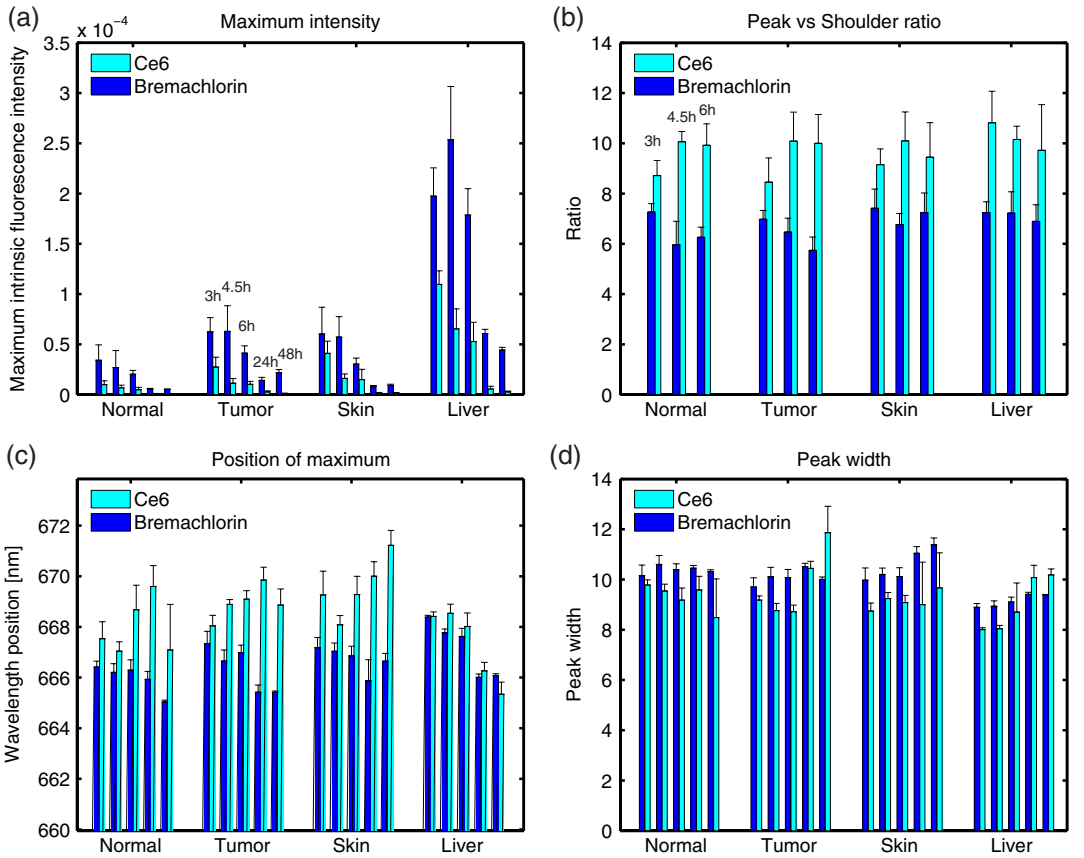

Fig. 8 (a) Maximum value of intrinsic fluorescence spectrum. This parameter correlates with the product of photosensitizer absorption coefficient and quantum yield at the peak wavelength. (b) Ratio between maximum value of intrinsic fluorescence spectrum and the fitted intensity parameter of the skewed Gaussian. This represents the ratio between peak and shoulder of the ce6/Bremachlorin fluorescence spectrum. (c) Wavelength that represents maximum intrinsic fluorescence peak position. (d) FWHM of the Gaussian representing the main intrinsic fluorescence peak.

4.1 *Spectral Variability in ce6*

It has been shown *in vitro* that both the fluorescence peak intensity and the peak position of ce6 are strongly influenced by pH of the solution.[32] For ce6 in PBS, a decrease in pH in the range of 7.5 to 3.5 results in a peak shift from 661 to 647 nm, combined with a decrease in intensity of the main fluorescence peak when the spectrum is normalized at 720 nm.[32] The range of peak positions for ce6 that we have observed was in the range of 665 to 671 nm, which is higher than reported by Cunderliková et al. It is shown for the spectral properties of ce6 in more physiologically relevant environments containing serum (by adding FCS, BSA, LDL/HDL) or measured *in vivo* that the binding of ce6 significantly shifts the peak position to higher wavelengths.[40] Studies of ce6 or ce6 conjugates in solution show a peak wavelength range comparable with what was found in this study.[35,40,49] Changes in pH influence binding affinity and thus the spectral shape represent the relative contributions of the differently bound ce6. The data in Figs. 8(b) and 8(c) showed a trend of increasing peak/shoulder ratio corresponding with increasing peak position wavelength in time after photosensitizer injection for tumor, normal tissue, and skin. According to Cunderliková et al.,[32] the increase of peak/shoulder ratio and peak position suggests a transition into a higher pH environment in an *in-vitro* situation. In the range of biological relevant pH values, the peak shift associated with pH variations is small. How this transfers to the *in-vivo* situation remains to be determined.

4.2 *Comparison of ce6 and Bremachlorin*

It is clear from Figs. 8(b) and 8(c) that although ratio and peak position increased for ce6, Bremachlorin showed the opposite; a blue shift in peak position accompanied by a decrease in shoulder ratio. This might suggest relocalization of the drug to an environment with a lower pH. Furthermore, binding of ce6 to low-density lipoproteins is also linked with a blue-shift of the peak position, compared to albumin bound ce6. This suggests that ce6 in Bremachlorin may be preferably bound to these LDL proteins, providing for uptake in (malignant) cells. Unbound ce6 is mainly accumulated in the plasma membrane of cells. The width of the peak, which could also be associated with pH, did not change significantly.

Bremachlorin consists of a mixture of chlorin e6, purpurin 5, and chlorin p6, in which both ce6 and purpurin 5 are known to have the photodynamic effect. In the administered mixture, ce6 also acts as a solvent, since purpurin 5 is too hydrophobic to be administered in aqueous solution. Purpurin has a high-binding affinity to low-density lipoproteins, allowing the drug to enter malignant cells via endocytosis.[50] Since ce6 accounts for the largest fraction in Bremachlorin, we expected the spectral shape to be dominated by ce6. The influence of the other

two components, purpurin 5 and chlorin p6, on the spectral shape and behavior is unknown. Both purpurin 5 and chlorin p6 are known to have an emission spectrum similar to ce6 when analyzed separately.[51,52] Our results showed that a mixture of ce6, cp6, and purpurin 5 clearly behaved differently than pure ce6. Bremachlorin is more lipophilic than pure ce6,[42] and it is therefore expected that the localization of Bremachlorin differs from pure ce6. It could not be determined from this experiment if the spectral variations between Bremachlorin and ce6 were a result of spectral influences of the two extra components, or if they were variations in ce6 spectra caused by changes in environment. However, our experiments did show that Bremachlorin has different spectral properties than pure ce6 and should therefore be investigated as a new photosensitizer, including optimization of the treatment protocol.

4.3 *Fluorescence Correction Method*

The method to use MDSFR for measuring the absorption and reduced scattering *in vivo* to recover the intrinsic photosensitizer fluorescence is developed based on the use of Monte-Carlo simulations and phantom studies. In these optimized circumstances, theory is validated and empirical parameters are included in the model.[23] However, applying this method *in vivo* is much less straightforward considering spatial heterogeneity and the potential for the confounding effects of tissue layers. In this study, MDSFR was performed using consecutive placement of two fiber diameters on the same spot. Therefore, slight differences in measurement volume were not only due to different fiber diameters but could also occur from measuring a slightly different sampling volume in each measurement. Therefore, the μ_s' used to correct the fluorescence was based on an average value and did not necessarily exactly represent the μ_s' in the fluorescence sample volume. New technological developments should overcome this problem in the near future and provide true colocalized measurement positions for various fiber diameters. Although we repositioned the probe on each tissue up to five times per mouse, the variation of variables compared within measurements of one mouse was at least four times smaller than the maximum variation between animals. Therefore, the size of the error bars was predominately due to interanimal variations.

4.4 *Implications and Future Work*

In this work, we have investigated spectral variations of chlorin e6 and Bremachlorin. Clear differences were observed in fluorescence intensity, peak/shoulder ratio and peak position for both sensitizers over time after injection. Furthermore, although Bremachlorin consists of approximately 80% of ce6, spectra showed distinct differences, suggesting variations in localization and/or clearance pathways. The more blue-shifted peak of Bremachlorin, together with the wider peak, suggests Bremachlorin was bound to LDL proteins more than ce6. This might result in a higher uptake of the photosensitizer in the cell. It is shown that internalization of the photosensitizer results in more PDT-induced damage than photosensitizers located on the cell membrane.[53] Furthermore, this may explain the prolonged detection of significant amounts of photosensitizer fluorescence in tissue compared to ce6.

Although results in this study look promising for using the ce6 in Bremachlorin as photosensitizer, purpurin 5 is known to have strong photodynamic activity as well. Spectral analysis showed us mainly variations in ce6. How this ce6 behavior relates to behavior and localization of purpurin 5 and influences PDT outcome remains to be investigated. In future studies, we aim to analyze the microscopic distribution of ce6 and Bremachlorin in tongue/tumor tissue.

5 Conclusion

In the present study, we used for the first time our quantitative SFF spectroscopy technique *in vivo* to analyze fluorescence spectra of both ce6 and Bremachlorin *in vivo*. Influence of optical properties on fluorescence varied up to 35% over the visible wavelength range and was tissue dependent. We analyzed variations of the spectral shape of the intrinsic fluorescence in normal tongue tissue, OSC tongue tumor, skin, and liver at $t = [3, 4.5, 6, 24, 48]$ h after photosensitizer injection. We observed significant differences in spectral shape over time between sensitizers. Although the wavelength position of the fluorescence intensity maximum underwent a red-shift over time for ce6, Bremachlorin showed a blue shift. Furthermore, the Bremachlorin peak appeared to be broader than the ce6 fluorescence peak. Intrinsic fluorescence intensity, which can be related to photosensitizer concentration, was decreasing for all time points but showed significantly more Bremachlorin present compared to ce6 at long incubation times. In conclusion, although Bremachlorin consists of ~80% of chlorin e6, they behaved significantly different *in-vivo*. These differences may be explored to define an optimal treatment protocol for Bremachlorin-based PDT.

Acknowledgments

We kindly thank Laura Mezzanotte for her work on the lentiviral transduction and production of the Luc2-gfp-OSC19 cell line, and the University Medical Centre Leiden for providing those cells for this study. We thank Dr. A. Reshetnickov for providing Bremachlorin.

References

1. I. Georgakoudi and J. Van Dam, "Characterization of dysplastic tissue morphology and biochemistry in Barrett's esophagus using diffuse reflectance and light scattering spectroscopy," *Gastrointest. Endosc. Clin. North Am.* **13**(2), 297–308 (2003).
2. R. Drezek et al., "Light scattering from cervical cells throughout neoplastic progression: influence of nuclear morphology, DNA content, and chromatin texture," *J. Biomed. Opt.* **8**(1), 7–16 (2003).
3. G. M. Palmer et al., "Quantitative diffuse reflectance and fluorescence spectroscopy: tool to monitor tumor physiology in vivo," *J. Biomed. Opt.* **14**(2), 024010 (2009).
4. A. Kim et al., "Quantification of in vivo fluorescence decoupled from the effects of tissue optical properties using fiber-optic spectroscopy measurements," *J. Biomed. Opt.* **15**(6), 067006 (2010).
5. N. N. Boustany, S. A. Boppart, and V. Backman, "Microscopic imaging and spectroscopy with scattered light," *Annu. Rev. Biomed. Eng.* **12**, 285–314 (2010).
6. P. Thueler et al., "In vivo endoscopic tissue diagnostics based on spectroscopic absorption, scattering, and phase function properties," *J. Biomed. Opt.* **8**(3), 495–503 (2003).
7. V. Ntziachristos, "Going deeper than microscopy: the optical imaging frontier in biology," *Nat. Methods* **7**(8), 603–614 (2010).
8. N. Kollias, G. Zonios, and G. N. Stamatas, "Fluorescence spectroscopy of skin," *Vib. Spectrosc.* **28**(1), 17–23 (2002).
9. D. J. Robinson et al., "Protoporphyrin IX fluorescence photobleaching during ALA-mediated photodynamic therapy of UVB-induced tumors in hairless mouse skin," *Photochem. Photobiol.* **69**(1), 61–70 (1999).
10. D. J. Robinson et al., "Fluorescence photobleaching of ALA-induced protoporphyrin IX during photodynamic therapy of normal hairless

mouse skin: the effect of light dose and irradiance and the resulting biological effect," *Photochem. Photobiol.* **67**(1), 140–149 (1998).
11. B. Karakullukcu et al., "Clinical feasibility of monitoring mTHPC mediated photodynamic therapy by means of fluorescence differential path-length spectroscopy," *J. Biophotonics* **4**(10), 740–751 (2011).
12. D. J. Robinson et al., "Optical spectroscopy to guide photodynamic therapy of head and neck tumors," *IEEE J. Sel. Top. Quantum Electron.* **16**(4), 854–862 (2010).
13. J. C. Finlay and T. H. Foster, "Recovery of hemoglobin oxygen saturation and intrinsic fluorescence with a forward-adjoint model," *Appl. Opt.* **44**(10), 1917–1933 (2005).
14. J. Wu, M. S. Feld, and R. P. Rava, "Analytical model for extracting intrinsic fluorescence in turbid media," *Appl. Opt.* **32**(19), 3585–3595 (1993).
15. M. G. Müller et al., "Intrinsic fluorescence spectroscopy in turbid media: disentangling effects of scattering and absorption," *Appl. Opt.* **40**(25), 4633–4646 (2001).
16. Q. Zhang et al., "Turbidity-free fluorescence spectroscopy of biological tissue," *Opt. Lett.* **25**(19), 1451–1453 (2000).
17. K. R. Diamond, M. S. Patterson, and T. J. Farrell, "Quantification of fluorophore concentration in tissue-simulating media by fluorescence measurements with a single optical fiber," *Appl. Opt.* **42**(13), 2436–2442 (2003).
18. H. Stepp et al., "Measurement of fluorophore concentration in turbid media by a single optical fiber," *Med. Laser Appl.* **22**(1), 23–34 (2007).
19. A. Amelink et al., "Quantitative fluorescence spectroscopy in turbid media using fluorescence differential path length spectroscopy," *J. Biomed. Opt.* **13**(5), 054051 (2008).
20. B. W. Pogue and G. Burke, "Fiber-optic bundle design for quantitative fluorescence measurement from tissue," *Appl. Opt.* **37**(31), 7429–7436 (1998).
21. U. A. Gamm et al., "Measurement of tissue scattering properties using multi-diameter single fiber reflectance spectroscopy: in silico sensitivity analysis," *Biomed. Opt. Express* **2**(11), 3150–3166 (2011).
22. U. A. Gamm et al., "Quantification of the reduced scattering coefficient and phase-function-dependent parameter Gamma of turbid media using multidiameter single fiber reflectance spectroscopy: experimental validation," *Opt. Lett.* **37**(11), 1838–1840 (2012).
23. S. Kanick et al., "Semi-empirical model of the effect of scattering on single fiber fluorescence intensity measured on a turbid medium," *Biomed. Opt. Express* **3**(1), 137–152 (2012).
24. S. C. Kanick et al., "Monte Carlo analysis of single fiber reflectance spectroscopy: photon path length and sampling depth," *Phys. Med. Biol.* **54**(22), 6991–7008 (2009).
25. S. C. Kanick, H. Sterenborg, and A. Amelink, "Empirical model of the photon path length for a single fiber reflectance spectroscopy device," *Opt. Express* **17**(2), 860–871 (2009).
26. F. Bevilacqua and C. Depeursinge, "Monte Carlo study of diffuse reflectance at source-detector separations close to one transport mean free path," *J. Opt. Soc. Am. A* **16**(12), 2935–2945 (1999).
27. S. C. Kanick et al., "Extraction of intrinsic fluorescence from single fiber fluorescence measurements on a turbid medium," *Opt. Lett.* **37**(5), 948–950 (2012).
28. H. S. de Bruijn et al., "Microscopic localisation of protoporphyrin IX in normal mouse skin after topical application of 5-aminolevulinic acid or methyl 5-aminolevulinate," *J. Photochem. Photobiol. B* **92**(2), 91–97 (2008).
29. A. Amelink et al., "Monitoring PDT by means of superficial reflectance spectroscopy," *J. Photochem. Photobiol. B* **79**(3), 243–251 (2005).
30. T. A. Middelburg et al., "Topical hexylaminolevulinate and aminolevulinic acid photodynamic therapy: complete arteriole vasoconstriction occurs frequently and depends on protoporphyrin IX concentration in vessel wall," *J. Photochem. Photobiol. B. Biol.* **126**, 26–32 (2013).
31. J. S. Nelson, W. G. Roberts, and M. W. Berns, "In vivo studies on the utilization of mono-L-aspartyl chlorin (NPe6) for photodynamic therapy," *Cancer Res.* **47**(17), 4681–4685 (1987).
32. B. Cunderlíková, L. Gangeskar, and J. Moan, "Acid-base properties of chlorin e6: relation to cellular uptake," *J. Photochem. Photobiol. B* **53**(1), 81–90 (1999).
33. H. Mojzisova et al., "Cellular uptake and subcellular distribution of chlorin e6 as functions of pH and interactions with membranes and lipoproteins," *Biochimica et Biophysica Acta Biomembranes* **1768**(11), 2748–2756 (2007).
34. G. Kostenich, I. Zhuravkin, and E. Zhavrid, "Experimental grounds for using chlorin e6 in the photodynamic therapy of malignant tumors," *J. Photochem. Photobiol. B* **22**(3), 211–217 (1994).
35. A. Orenstein et al., "A comparative study of tissue distribution and photodynamic therapy selectivity of chlorin e6, Photofrin II and ALA-induced protoporphyrin IX in a colon carcinoma model," *Br. J. Cancer* **73**(8), 937–944 (1996).
36. W. W. L. Chin et al., "Fluorescence imaging and phototoxicity effects of new formulation of chlorin e6-polyvinylpyrrolidone," *J. Photochem. Photobiol. B* **84**(2), 103–110 (2006).
37. S. W. Taber et al., "Photodynamic therapy using mono-L-aspartyl chlorin e6 (Npe6) for the treatment of cutaneous disease: a Phase I clinical study," *Clin. Cancer Res.* **4**(11), 2741–2746 (1998).
38. R. A. Lustig et al., "A multicenter Phase I safety study of intratumoral photoactivation of talaporfin sodium in patients with refractory solid tumors," *Cancer* **98**(8), 1767–1771 (2003).
39. A. L. Chan et al., "Pharmacokinetics and clinical effects of mono-L-aspartyl chlorin e6 (NPe6) photodynamic therapy in adult patients with primary or secondary cancer of the skin and mucosal surfaces," *Photodermatol. Photoimmunol. Photomed.* **21**(2), 72–78 (2005).
40. S. Douillard et al., "In vitro evaluation of Radachlorin sensitizer for photodynamic therapy," *J. Photochem. Photobiol. B* **98**(2), 128–137 (2010).
41. S. Douillard, D. Olivier, and T. Patrice, "In vitro and in vivo evaluation of Radachlorin sensitizer for photodynamic therapy," *Photochem. Photobiol. Sci.* **8**(3), 405–413 (2009).
42. A. Uzdensky et al., "Photodynamic effect of novel chlorin e6 derivatives on a single nerve cell," *Life Sci.* **74**(17), 2185–2197 (2004).
43. F. van Leeuwen-van Zaane et al., "In vivo quantification of the scattering properties of tissue using multi-diameter single fiber reflectance spectroscopy," *Biomed. Opt. Express* **4**(5), 696–708 (2013).
44. U. A. Gamm et al., "Extraction of intrinsic fluorescence from single fiber fluorescence measurements on a turbid medium: experimental validation," *Biomed. Opt. Express* (2014) in press.
45. C. L. Hoy et al., "Use of a coherent fiber bundle for multi-diameter single fiber reflectance spectroscopy," *Biomed. Opt. Express* **3**(10), 2452–2464 (2012).
46. T. Yokoi et al., "Establishment and characterization of a human cell line derived from a squamous cell carcinoma of the tongue," *Tumor Res.* **23**, 43–57 (1988).
47. F. Carlotti et al., "Lentiviral vectors efficiently transduce quiescent mature 3T3-L1 adipocytes," **9**(2), 209–217 (2004).
48. L. Mezzanotte et al., "Evaluating reporter genes of different luciferases for optimized in vivo bioluminescence imaging of transplanted neural stem cells in the brain," *Contrast Media & Mol. Imaging* **8**(6), 505–513 (2013).
49. S. Mitra and T. H. Foster, "In vivo confocal fluorescence imaging of the intratumor distribution of the photosensitizer mono-L-aspartylchlorin-e6," *Neoplasia* **10**(5), 429–438 (2008).
50. G. Jori and E. Reddi, "The role of lipoproteins in the delivery of tumour-targeting photosensitizers," *Int. J. Biochem.* **25**(10), 1369–1375 (1993).
51. G. M. Garbo, "Purpurins and benzochlorins as sensitizers for photodynamic therapy," *J. Photochem. Photobiol. B* **34**(2), 109–116 (1996).
52. E. Zenkevich et al., "Photophysical and photochemical properties of potential porphyrin and chlorin photosensitizers for PDT," *J. Photochem. Photobiol. B* **33**(2), 171–180 (1996).
53. P. Agostinis et al., "Photodynamic therapy of cancer: an update," *CA Cancer J. Clin.* **61**(4), 250–281 (2011).

Biographies of the authors are not available.